Earth and Planetary Science Letters 600 (2022) 117871

Contents lists available at ScienceDirect

Earth and Planetary Science Letters

www.elsevier.com/locate/epsl

Using active source seismology to image the Palos Verdes Fault damage zone as a function of distance, depth, and geology

Travis Alongi [a,*], Emily E. Brodsky [a], Jared Kluesner [b], Daniel Brothers [b]

[a] University of California, Santa Cruz, United States of America
[b] U.S. Geological Survey, Santa Cruz, United States of America

ARTICLE INFO

Article history:
Received 7 June 2022
Received in revised form 13 October 2022
Accepted 15 October 2022
Available online xxxx
Editor: J.-P. Avouac

Dataset link: https://walrus.wr.usgs.gov/NAMSS/

Keywords:
fault damage zone
active source reflection seismology
fault imaging & detection

ABSTRACT

Fault damage zones provide a window into the non-elastic processes of an earthquake. Geological and seismic tomography methods have been unable to measure damage zones at depth with sufficient spatial sampling to evaluate the relative influence of depth, distance, and lithological variations. Here, we identify and analyze the damage zone of the Palos Verdes Fault offshore southern California using two 3D seismic reflection datasets. We apply a novel algorithm to identify discontinuities attributed to faults and fractures in large seismic volumes and examine the spatial distribution of fault damage in sedimentary rock surrounding the Palos Verdes Fault. Our results show that damage through fracturing is most concentrated around mapped faults and decays exponentially to a distance of ~2 km, where fracturing reaches a clearly defined and relatively undamaged background for all examined depths and lithologies (450 m to 2.2 km). This decrease in fracturing with distance from the central fault strand exhibits similar functional form to outcrop studies. However, here we extend analysis to distances seldom accessible (~10 km lateral distance). Separating the data by geologic units we find that the damage decay and background level differs for each unit, with the older and deeper units having higher levels of background fracturing and shallower exponential decays of fracturing with distance from the fault. Surprisingly, these differences in damage decay and background level trade-off result in a consistent damage zone width regardless of lithology or depth. We find that the damage zone has similar decay trends on both sides of the fault. When examining the damage zone at shorter (4 km vs 17 km) along strike distances, the damage zone has a more complex decay trend and at least two strands are resolvable.

1. Introduction

Earthquakes release accumulated elastic strain energy. Part of that energy is consumed in the fracturing of rock both on the fault and in the surrounding damage zone. The damage zone is broadly defined as the area where fracture density is higher than the surrounding background fracture density (Chester and Logan, 1986; Kim et al., 2004; Mitchell and Faulkner, 2009; Faulkner et al., 2010) and forms a halo of increased fracturing around the highly localized principal slip surface (Chester and Logan, 1986; Caine et al., 1996; Choi et al., 2016; Rodriguez Padilla et al., 2022). Damage zones are significant in earthquake physics for at least four reasons. First, the damage process itself is potentially a sink of energy during earthquake rupture (Wong, 1982; Martel and Pollard, 1989; Wilson et al., 2003; Chester et al., 2005; Abercrombie and Rice, 2005; Brodsky et al., 2020). Constraining the extent of the damage zone at depth is important for evaluating the relative importance of fracture energy in the overall energy budget of the fault system. Secondly, damage zones are highly permeable and particularly important in controlling the distribution and mobility of fluids around faults (Caine et al., 1996). Since fluid pressure can be a major factor in earthquake nucleation (King Hubbert and Rubey, 1959), understanding the structure of the damage zone is a prerequisite for modeling how fluid flow can contribute to initiating and propagating earthquakes. Thirdly, the rheology of the damage zone is distinct from the surrounding media and plastic deformation in the damage zone can alter the rupture dynamics of an earthquake (Dunham et al., 2011; Thakur et al., 2020). Finally, the extent of the damage zone reflects the aggregate seismic deformation across a particular fault and thus could potentially be used to guide hazard investigations. Offset features are typically measured over a relatively narrow width on either side of the fault and may not capture all of the coseismic deformation and thus measuring damage provides a potentially important alterna-

* Corresponding author.
E-mail address: talongi@ucsc.edu (T. Alongi).

https://doi.org/10.1016/j.epsl.2022.117871
0012-821X/

tive window into the seismic history. Establishing the extent of the damage zone in three-dimensional (3D) space is therefore an important goal for both fundamental science and pragmatic reasons.

Despite its importance, basic knowledge of the systematics of the 3D damage zones is limited, and much of what is known is from geologic outcrop exposures and related observations (Scholz et al., 1993; Wilson et al., 2003; Shipton et al., 2006; Mitchell and Faulkner, 2009; Savage and Brodsky, 2011; Keren and Kirkpatrick, 2016). In these studies, the damage zone width has been shown to scale nonlinearly with various fault parameters such as length, displacement or throw, and number of strands (Childs et al., 1997; Cowie and Shipton, 1998; Savage and Brodsky, 2011; Torabi and Berg, 2011). Outcrop studies of exhumed fault zones and surface rupture are limited to surficial measurements of fracture density and lack the means to quantify the damage in-situ at depth. Limited availability of fault exposures has made it difficult to disentangle the contributions of lithology, depth, and distance from the fault. Undoubtedly all three factors play a role in controlling the relative damage, but they are seldom separable in outcrop studies.

Passive seismic data have provided some insights on the in-situ fault damage zones. Some studies have shown a reduction in seismic body wave velocities near faults and were interpreted to be due to reduced elastic moduli, a proxy for damage (Ben-Zion et al., 2003; Vidale and Li, 2003; Cochran et al., 2009;). However, these studies are limited by access and deployment logistics on land as well as sparse and often clustered earthquake sources to sample the fault zones. Extent and velocity changes often trade-off in inversion methods, thus establishing variations with depth, distance and lithology are again challenging by these methods.

Active source marine seismic data can provide a higher-resolution view of the fault damage zone because they do not rely on proxies to infer elastic moduli and is a more direct approach for detecting faults and fractures. Three-dimensional seismic reflection techniques, typically used in hydrocarbon exploration, have long been used to infer faulting in-situ through offsets in reflectors. Similarity attributes have been used to improve and guide the interpretation of faults in seismic data (Bahorich and Farmer, 1995; Marfurt et al., 1998; Chopra and Marfurt, 2005). These methods use measures of multi-trace similarity over a moving window and have been validated with forward modeled synthetic faults in seismic volumes (Botter et al., 2016). Faults have been identified using similarity attribute methods (Iacopini et al., 2016) and subsequently used to study the fault damage zone on fault perpendicular cross sections in seismic volumes (Torabi et al., 2017; Liao et al., 2019; Ma et al., 2019). Rather than analyzing the damage zone at representative cross sections, the present study aims to examines the damage zone in the full 3D volume. Additionally, machine learning approaches have implemented supervised neural networks to set the weights of ensembles of discontinuity-detecting attributes to highlight faults and possible fluid pathways associated with fault junctions (Kluesner and Brothers, 2016).

Here we apply a previously developed modern fault detection and localization algorithm to existing 3D marine seismic data along the Palos Verdes Fault to extract a 3D fault network from the data. Prior studies have suggested that fracture density follows well-defined statistical distributions that need to be well-sampled in order to be quantified (Mitchell and Faulkner, 2009; Savage and Brodsky, 2011). Reflection seismic data provide a powerful way to define these distributions using averaging in large volumes to seek generalizable behavior. We follow this approach by detecting fractures, measuring systematics, averaging volumes, and then pursuing the spatial and lithological controls on damage.

2. Tectonic setting and data

2.1. Palos Verdes Fault in context

The Palos Verdes Fault (PVF) is mainly located offshore southern California in the Inner Continental Borderland and accommodates a portion of the distributed shear zone between the Pacific and North American Plates (Fig. 1). Current estimates suggest that the California Borderland accommodates 6–8 mm/yr of right lateral motion, and the Palos Verdes Fault slip rate is between 1.6–4 mm/yr (Ward and Valensise, 1994; McNeilan et al., 1996; Brankman and Shaw, 2009; Brothers et al., 2015). The northwest southeast striking fault stretches over 100 km in length, from Lausen Knolls in the south to Santa Monica Bay in the north and its connectivity with other faults remains a topic of interest. The Palos Verdes Fault has very few recorded earthquakes in the San Pedro Shelf region (Fig. 1). Uncertainties in fault dip and connectivity to nearby faults yield uncertainty in maximum earthquake magnitude potential (Mw 6.5–7.5). There is clear vertical separation of the sedimentary units across the fault where units west of the fault are closer the seafloor, and there is decreasing vertical separation toward the south. Seismic data show that the fault is near-vertical in the upper 2 km, but debate continues about whether the fault becomes listric at depth (Fisher et al., 2004; Brankman and Shaw, 2009; Brothers et al., 2015). It has been suggested that the Palos Verdes Fault soles into a master décollement below the Los Angeles basin and may be a component of a larger fault system (Webb and Kanamori, 1985; Hubbard et al., 2014).

The geological history of the region is largely controlled by the transition from a convergent to transform plate boundary that occurred as the Farallon Plate was completely subducted beneath the North American Plate during the Oligocene (∼30 Ma) (Atwater, 1970; Bohannon and Geist, 1998). The plate boundary transition led to several stages of faulting, deformation, and stress reorientation over the history of the Palos Verdes Fault. Pre-Miocene Borderland (∼25 Ma) tectonics are characterized by flat slab subduction and intense contact metamorphism. By the early Miocene (∼23 Ma) the margin had reorganized to transform tectonics, and that was followed by late-Miocene oblique extension, leading to rifting of the Borderland and vertical axis clockwise block rotation of the western transverse ranges (Crouch and Suppe, 1993). Seismic stratigraphy of Monterey Formation sediments suggests that the Palos Verdes Fault was active by at least the middle to late Miocene (∼15 Ma) (Brankman and Shaw, 2009; Sorlien et al., 2013). In the early Pliocene (∼6 Ma) the plate boundary stepped inland and created a major left step restraining bend (known as the Big Bend) changing the Borderlands from a transtensional to a transpressional system. This transition led to reactivation of extensional normal faults as oblique thrust faults (Yeats and Beall, 1991; Wright, 1991). The existence of the uplifted Palos Verdes Peninsula anticlinorium and associated marine terraces suggests that this topography is supported by oblique convergence (Plesch et al., 2007), a transpressional restraining bend, or a combination of the two (Ward and Valensise, 1994; Shaw and Suppe, 1996; Fisher et al., 2004; Sorlien et al., 2013). The geologic history includes the superposition of several different tectonic and stress regimes that cumulatively contribute to the damage zone. There is a clear difference in the deformation history on the west versus east side of the Palos Verdes Fault. The anticline west of the fault appears to be decoupled from the relatively horizontal sediments in the basin east of the fault that are observable in the data to ∼10 km from the fault.

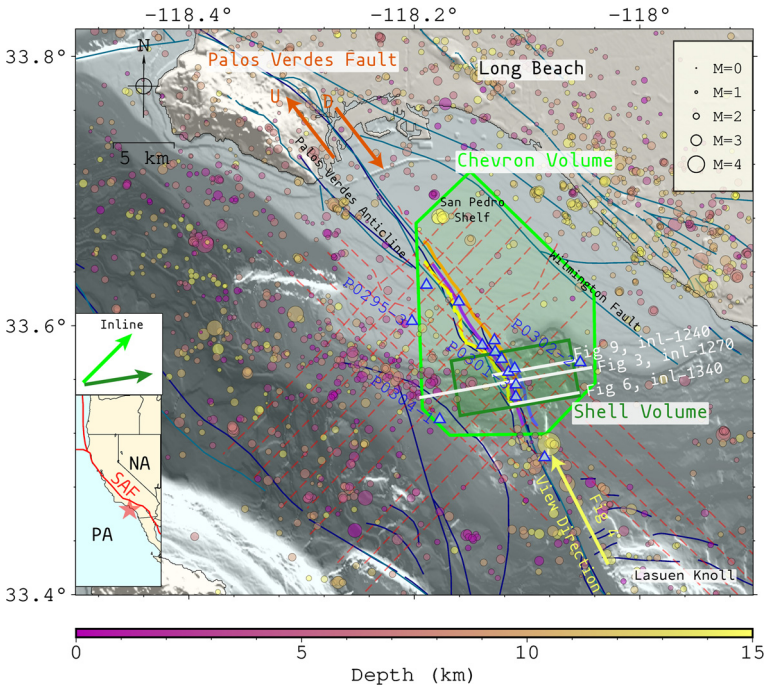

Fig. 1. Map of southern California Inner Continental Borderland and San Pedro Shelf. Inset map shows western North America with the red star indicating the study area offshore southern California, NA - North American Plate, PA – Pacific Plate, SAF – San Andreas Fault. Main map shows location of mapped fault traces, where the navy-blue lines are mapped offshore Quaternary faults (Walton et al., 2020) and the turquoise lines are onshore Quaternary faults (U.S. Geological Survey and California Geologic Survey, Quaternary fault and fold database for the United States, accessed August 2019). The green polygons depict the bounds of the three-dimensional (3D) marine active source datasets, lime green for Chevron volume and forest green for Shell volume. The solid yellow, purple, orange, and blue lines within the seismic volume footprint are the western, central, eastern and eastern 2 fault strands respectively mapped in this study. Dashed red lines indicate the two-dimensional (2D) lines used in the study. The blue triangles indicate the surface location of the geophysical well logs, named logs are outside of the fault zone and referred to in the text. White lines are the location of cross-sections of lines shown in other figures. Yellow arrow is the view direction from Fig. 4. Circles represent earthquakes colored by depth (purple to yellow, shallow to deep) and scaled by magnitude from the Southern California Earthquake Data Center alternate catalog [1981–2018] (Hauksson et al., 2012). (For interpretation of the colors in the figure(s), the reader is referred to the web version of this article.)

2.2. Data

To examine the damage zone in-situ we utilize existing marine seismic reflection data that are available through the USGS at the National Archive of Marine Seismic Surveys (Triezenberg et al., 2016). We use two overlapping legacy exploration 3D marine seismic reflection datasets along with 2D multi-channel seismic lines collected offshore of Los Angeles over the San Pedro shelf and slope, spanning ~17 km along strike distance of the Palos Verdes Fault (Fig. 1). The larger of the two seismic volumes survey is bound by a 7-sided polygon with a 350 km^2 footprint and was collected by Unocal in 1976 (C-01-76SC-3D). The airgun seismic source was recorded by a multichannel streamer sampling at 4 ms with bin spacings of 50 m and 25 m in the inline and crossline directions, respectively. Additionally, we analyze a smaller higher spatial density dataset collected by Shell in 1984 (B-388-84SC-3D) that overlaps the Chevron volume. The 69 km^2 survey footprint is rectangular and oriented with the longer dimension sub-parallel to the shelf break and nearly perpendicular to the Palos Verdes Fault strike with bin spacings of 25 and 12.5 m, respectively in the inline and crossline directions. The seismic processing was previously completed on both volumes and are post-stack and migration was performed, with spectral ranges of 5–60 Hz. Additionally, the data had gain correction applied to equalize the intrinsically attenuated signal with depth before public release.

In addition to the 3D seismic data, we use higher resolution 2D airgun multi-channel seismic lines that intersect the 3D volumes to quality check structural and stratigraphic features observed within the 3D volumes. The 2D profiles were collected by WesternGeco in 1981 (W-30-81SC-2D, 20 m shot spacing, 6 s record length, 4 ms sample rate). Lastly, we use exploratory geophysical well logs and lithology logs (Fig. 1 & S1) that were acquired from the Bureau of Safety and Environmental Enforcement through a Freedom of Information Act request (see Supplement). In order to incorporate well lithology logs recorded in depth into the seismic volumes in two way travel time 1D velocity models were calculated for each well located within the volume (see Supplement & Figure S1). With well lithology logs (unconformity contacts) converted to two-way travel time seismic horizons could be mapped within the 3D volumes.

3. Methods & results

3.1. Data conditioning

The methods and workflow are outlined schematically in Fig. 2A. First, all seismic SEGY navigation headers were converted from North American Datum 1927 State Plane Zone 6 to Universal Transverse Mercator Zone 11 N and imported into seismic interpretation software, OpendTect. The seismic data were pre-processed using dip-steered diffusion filtering in order to reduce noise and increase lateral continuity of reflectors while retaining discontinuities (Chopra and Marfurt, 2008). This attribute applies median filtering in a moving 3D window (inline, crossline, and time-window) following structural dip in areas with shallow to moderate dipping reflectors and areas with very steep dips are not median filtered. This approach reduces smearing of median filtering across faulting discontinuities and retains sharp images of faults (Marfurt et al., 1998; Tingdahl and De Rooij, 2005). The Palos Verdes Fault is clearly delineated by vertical offset of reflectors and folding surrounding the fault (Fig. 3).

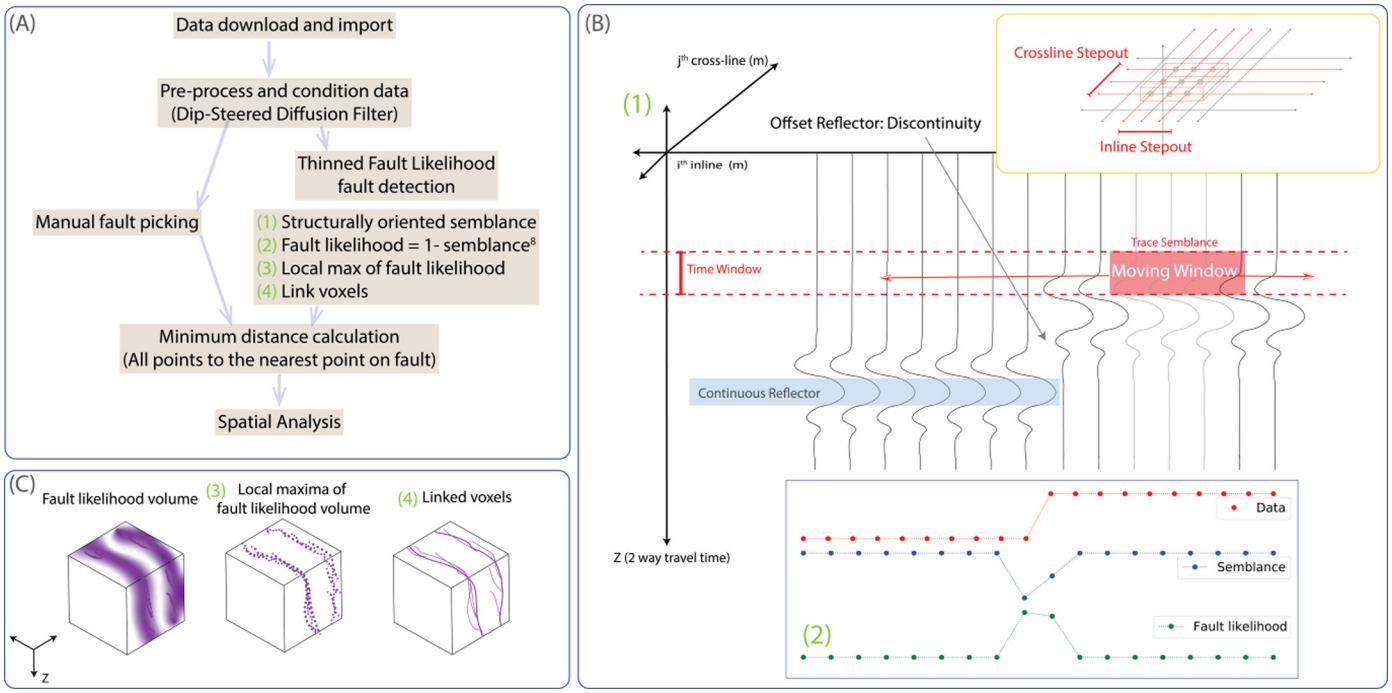

Fig. 2. (A) workflow diagram; the green numbers correspond to the steps illustrated in panels B & C. (B) Cartoon diagram of fault likelihood volume calculation (following Hale (2013)) based on a semblance volume, where semblance is a measure of multi-trace similarity among adjacent traces within a time window that is structurally oriented by dip-steering (see text for details). The upper inset shows a three-dimensional (3D) moving window over inline, crossline and two-way travel time; the lower inset depicts the fault-likelihood of this moving window. (C) Illustration of the steps that result in a linked, 3D fault and fracture network, including local maxima and linked discontinuity volumes.

3.2. Manual fault mapping & horizon mapping

Three dominant fault strands that are a spatial reference for the study were manually mapped throughout the volume in the sedimentary rock. The fault could be mapped continuously with high confidence in the depth range 350 m—2.2 km, we selected this depth range to avoid low signal-to-noise in the basement (depth $>$ 2.2 km), and processing artifacts related to multiple suppression in the shallow section ($<$500 ms two-way travel time). High resolution 2D seismic lines were used to guide manual picking and for quality control (Fig. 1, S2). The first fault picking pass was completed picking on 500 m spaced inlines (roughly perpendicular to fault) then refined using the combined 2D and 3D datasets (Figure S2). The fault picks were interpolated to form three continuous 3D fault surfaces which is consistent with detailed geomorphic and sub-bottom mapping (Brothers et al., 2015; Walton et al., 2020).

Six key horizons were mapped throughout the volumes, in order to evaluate the damage zone by sedimentary lithology. These horizons were carefully constrained in depth by tying to lithologic boundaries identified in 13 lithological and paleontological well logs (Fig. 1, S1, S3). The lithology contacts in measured depth were converted to two-way travel time by integrating the coincident velocity logs for each well and were then used as constraints on horizon mapping (Figure S3). Horizon mapping was done by manually picking laterally continuous reflectors that begin at well contacts that are outside of the fault zone and carefully mapping and connecting to well equivalent contacts within the fault zone, but not crossing the central fault strand. Six horizons (Pico Lower, Repetto Upper, Repetto Lower, Monterey Delmontian, Monterey Mohnian, and Catalina Schist Basement) were mapped east of the fault starting at well P0302-2 (Fig. 1) and are relatively flat lying throughout most of volume east of the fault, but are concave up near the fault. Only the 3 oldest contacts (Monterey Delmontian, Monterey Mohnian, and Catalina Schist Basement) were mappable west of the fault because the younger units have been uplifted with the Palos Verdes Anticline and subsequently eroded away (Wright, 1991; Sorlien et al., 2013). The mapping of the units on the west side of the fault started at wells P0304-1 and P0295-3 (Fig. 1) at the western edge of the Chevron volume, continuing east to the central fault strand. The morphology of the horizons west of the fault are more complex and folded as part of the anticline, with the axial surface sub-parallel to the Palos Verdes Fault and plunging to the southeast.

3.3. Automated fault detection

We use the thinned fault likelihood algorithm to automate identification of faults and fractures within both seismic volumes (Hale, 2013) and compare these results with the manually interpreted fault strands (Fig. 2). Thinned fault likelihood uses structurally guided semblance (a measure of multitrace similarity over a time-window) to scan adjacent traces and identify discontinuous regions, over a moving space-time window (Fig. 2b). Here we use a filter window size of 2 inline / 2 crossline and 32 ms. The local maxima of the semblance volume are preserved, thinning the discontinuous regions (Fig. 2c.). These local maxima voxels are then scanned over geologically reasonable dips and azimuths (strikes within +/-40 degrees of the Palos Verdes Fault and dips in the range of 70–89 degrees) for adjacent high dissimilarity voxels which are then linked, forming a fault and fracture network. An example of the results of thinned fault likelihood can be seen in Fig. 3. The resultant thinned fault likelihood volume has a likelihood (0-1) for each 3D voxel of being a fault or fracture.

3.4. Spatial analysis

To examine how fracturing varies spatially, we calculate the binned average probability of a fracture being present as a function of distance from the central fault strand and each of the horizons. Given the large dataset, efficient calculation of distances is important to implement. We calculate the minimum distance from

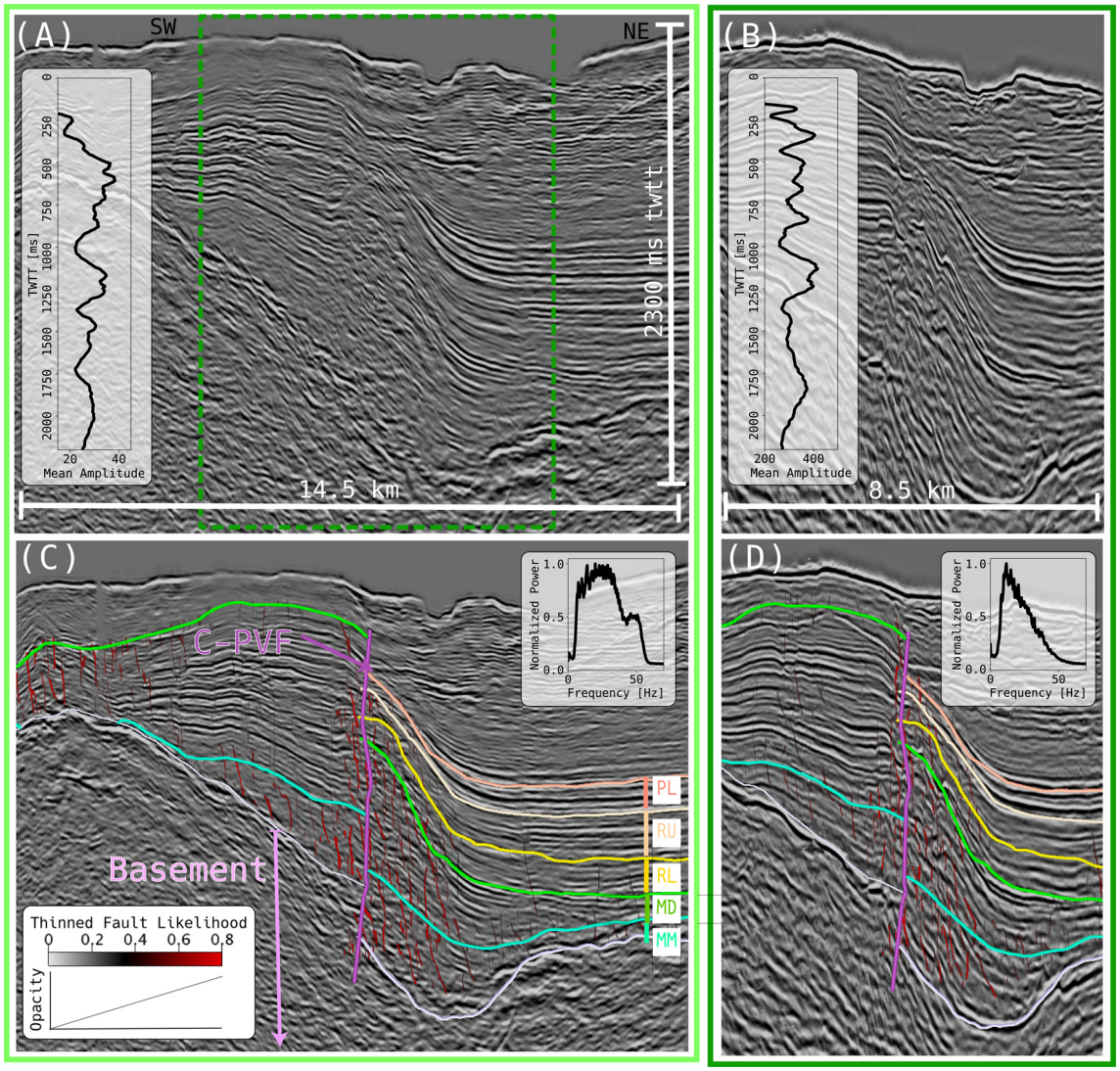

Fig. 3. Comparison of conditioned data and thinned fault likelihood results from overlapping portions of the Chevron (left panels) and the Shell (right panels) seismic volumes. Showing processed (dip-steered diffusion filtered) seismic inline number 1270 both uninterpreted (A & B) and with manual interpretation and fault detection (C & D). Map view of line location is shown in Fig. 1. The dashed dark green line in the (A) shows the extent of the Shell line. There is a 9000 m/s vertical exaggeration applied to help highlight the vertical offsets along the fault. The Palos Verdes Fault is clearly shown by offset reflectors, folding, and deformation features. (A & B) Dimensions are indicated by the white bars, and the inset indicates the mean amplitude as a function of two-way travel time (depth). (C & D) transparent to red overlay is the thinned fault likelihood attribute, where red is the high dissimilarity or high likelihood of being a fault. Purple sub-vertical line is the central Palos Verdes Fault strand (C-PVF) and the rainbow-colored sub-horizontal lines are three-dimensional (3D) horizons at the inline (PL - Pico lower, RU - Repetto upper, RL - Repetto lower, MD - Monterey Delmontian, MM - Monterey Mohnian). The inset shows the normalized power spectra for each survey.

each voxel ($N_{Chevron} = 4.8 \times 10^8$; $N_{Shell} = 1.2 \times 10^8$) in the volume to the mapped fault surface ($N = 2 \times 10^6$) and each of the horizons ($N = 8.9 \times 10^5$/horizon), using a nearest neighbor ball-tree approach. This is an unsupervised learning method designed to find a point in a given set that is closest (in this case, Euclidean distance) to the given point. The ball tree method subdivides the dataset into a tree structure of overlapping spheres that increases the efficiency of the nearest neighbor calculation. As with manual fault mapping (section 3.2), we limit our analysis to depth ranges of high-quality data that are above the basement and below the pico-middle/pico-lower unconformity due to low signal to noise ratios in the basement and artifacts introduced in the shallow subsurface due to multiple suppression efforts.

We bin the data spatially by distance from fault to examine spatial relationships of thinned fault likelihood probability. In each bin, the mean probability P is

$$< P >= \sum p_i / N \quad (1)$$

where p is the probability of the *ith* voxel being a fault (within prescribed spatial bin), N is the number of voxels in the spatial bin and angle brackets denote the mean. Note that the bins have varying numbers of voxels, thus the normalization by N is necessary. For conciseness, we will refer to the bin-averaged value P as simply fault probability for the rest of this study.

First, we examine the data as a function of this distance from the fault, to explore the lateral distance dependence of damage. The large number of data points ($\sim 10^8$) allows for narrow bin widths, here we use a bin width of 25 m and find that different bin sizes do not impact the results (Figure S4). Fig. 5 shows a clear relationship between fracture probability and lateral distance from the fault in which the fracture probability decays to a stable background value at 2 km distance from the central strand of the fault for both seismic volumes. This macroscopic damage zone is likely the superposition of the damage decays of all faults near the central strand (section 4.5). The data appear to obey exponential

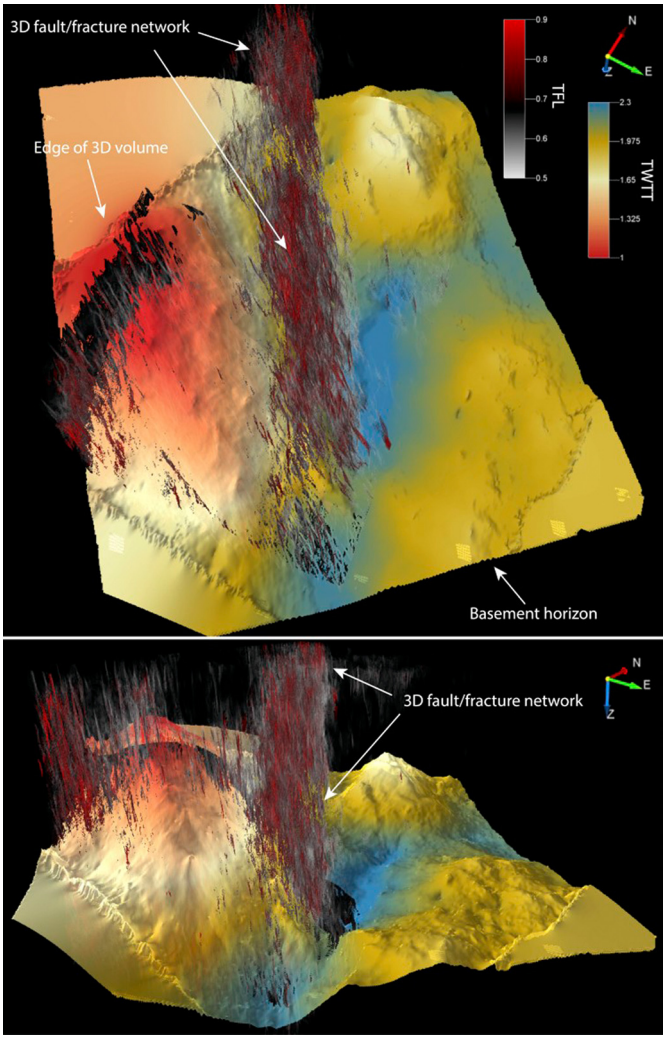

Fig. 4. Perspective view of thinned fault likelihood (TFL) attribute results for the Chevron volume along the Palos Verdes Fault Zone. The transparent to red color scale range indicates probability of a fault, where fault probabilities <0.6 are transparent. The basement horizon surface is shown with a blue to red color map indicating depth in two-way travel time (twtt in seconds). (top) Map view (bottom look direction pointed out in Fig. 1) is an along strike perspective view. Note the width variability of the damage zone along strike, and the complex detected fault geometry and structures.

scaling up to ~2 km, and can be well represented in this region by,

$$P = C10^{(-x/x0)} \quad (2)$$

where x is the perpendicular distance from the fault surface, $x0$ is an exponent that we will call the decay distance and C is a fault specific constant. A least square fit to the data yields $x0 = 3540$ m and 3200 m for the Chevron and Shell volumes, respectively. We calculate the background fracture probability, B as the mean of fracture probability of distances between 2000–3500 m. We bootstrapped the error on the parameters $x0, C$, and B, and these are provided in Table 1 (see Figure S5 & S6 for distributions).

Next, we investigate the effects of lithology on damage surrounding the fault. The mapped lithology contact horizons (see section 3.2) were used to constrain voxels in 3D space and to analyze fracturing between vertically adjacent horizon surfaces (Figure S7). We calculate fault probability binned by distance from the central fault, for each of the 5 sedimentary lithologies using equations (1) & (2). Fig. 6 shows the results, and each lithologic unit is again well fit by an exponential relationship, similarly to the bulk trend (Fig. 5), and the general decay and background trends are similar between the two volumes. There are unique exponential trends and background fracture probabilities for each unit. The larger Chevron volume represents 17 km along strike averaged results and the smaller Shell volume represents 4.5 km along strike and exhibits increased variance in the damage decay and the background, to be discussed more in section 4.4.

The pervasive fracturing observed in the Monterey Formation is consistent with previous studies that show that the Monterey Formation is brittle (Bramlette, 1946; Behl, 1999). There appears to be a tradeoff between damage decay and overall background damage (horizontal portion of the plots) that yield a remarkably consistent damage width (intersection of decay slope with background) in all units, which is discussed in greater detail in section 4.4.

Finally, we compare the damage zone on the east and west sides of the fault in the two Monterey units (Delmontian & Mohnian) that are mappable on both east and west sides of the fault (Fig. 7). We analyze the Delmontian and Mohnian, Monterey Formations, on an east versus west comparison and the results are shown in Fig. 8. Here we calculate the fault probability in the Chevron and Shell volumes over 11 km and 4.5 km of fault length, respectively. We find increased variability in the decay trends and the background as we examine shorter segments of the fault. The shorter fault length analyzed in the smaller Shell volume exhibits more complexity in the decay of fracturing with distance in the units. When we search for the optimal background distance D it becomes apparent that we are resolving 2 fault strands, which present as peaks in fracture probability at 0 and about 1 km distance east of the central fault strand. For the short 4.5 km section (Shell volume) of the fault we fit from the eastern trend using the peak in fracture probability east of the central fault strand (1 km distance away), while the western trend is fit with respect to the central strand. This results in east and west fits for the slopes X_o and distance cutoffs D that are similar on both sides of the fault.

4. Discussion

4.1. Validity of P as a measure of fracturing

The thinned fault likelihood method appears to successfully identify faults and fractures within the 3D seismic volumes (Fig. 3, 6 & 7) and identify features within the data that seismic interpreters would routinely identify as a fault zone, such as offset reflectors and change in reflection characteristics (Iacopini et al., 2016; Alcalde et al., 2017) (Fig. 3). Additionally, the highest fault likelihood regions localize around faults identified in this study and independent mapping efforts as the Palos Verdes Fault (Brankman and Shaw, 2009; Sorlien et al., 2013; Walton et al., 2020). There is also good agreement on the location and the identification of the damage zone with thinned fault likelihood in both 3D volumes and on the 2D seismic lines (Figure S2), that were independently collected and processed, reducing the possibility that the method is measuring a data artifact. Finally, the fundamental finding that fault probability is highest at the location of the primary fault strand supports the validity of using this method to measure fault structure.

4.2. Density - distance relationship

We find that the fracture probability decreases with distance from the fault and is best fit by an exponential curve, with a decay distance of ~3000 m. This observation is of the same functional form as those observed in outcrop studies though cannot be compared directly because of different metrics and methods used in fracture characterization (Faulkner et al., 2003; Mitchell and Faulkner, 2009). Distinguishing exponential and power-laws

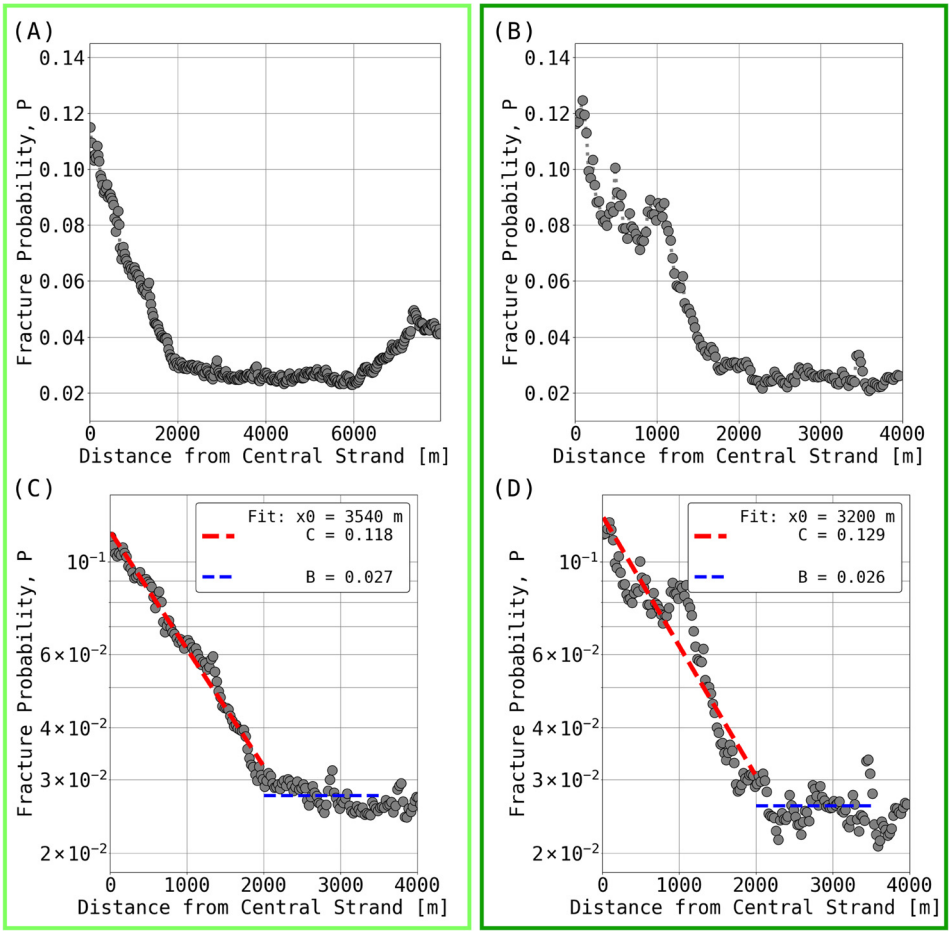

Fig. 5. (top) Fracture probability relationship with distance east of central mapped strand. Fracture probability decays with distance east from the central strand to ~2 km from the fault. (A & C) shows the Chevron volume results (B & D) show the Shell results. (A & B) are in linear space and (C & D) the Y-axis are in log space. The background, low fracture probability, begins at 2 km and at distances greater than 6 km fracturing likely increases due to the Wilmington Fault (and its damage zone, see Fig. 1) at the eastern edge of the seismic volumes. (C & D) Shows the exponential relationship between fracture density and distance from the central strand. Red line indicates the least squares exponential fit through the damaged region to 2.0 km, and the blue line shows the background level. The outer edges (2 km) were chosen as the clear change in slope. Variables x0 and C are defined in equation (2).

relationships is not straightforward, and it is advised to span several orders of magnitude before determining the appropriate functional form (e.g., Bonnet et al., 2001). Results from this study span 3 orders of magnitude (10^1–10^3 m) of distance and an order of magnitude of fault probability, and as we extend our study up to 8 km from the fault for the Chevron dataset and 4 km for the Shell dataset. These observations are at distances from the fault that are seldom accessible in outcrop studies (typically hundreds of meters in rare cases up to a few kilometers) (Faulkner et al., 2003; Savage and Brodsky, 2011). Seismic acquisition and binning results is a low-pass filter on the data and smaller scale fractures, commonly counted in outcrop transects, are not recoverable (see Supplement). Unique to this method and study is the clearly defined edge of the fault damage zone, which agrees with damage zone models, where the damage decay intersects a stable background (from tectonic stresses). This edge occurs at ~2 km east of the central strand (Fig. 5), and provides a robust distance cut off for fitting.

In this study the damage zone is examined fully in 3D and is not restricted to the 1D or 2D surfaces of previous surficial studies (Chester and Logan, 1986; Berg and Skar, 2005; Sagy and Brodsky, 2009). We show that the along-strike averaged faulting and fracture probability, over the depth ranges bound by the pico-lower and the basement contacts (~400–2200 m depth, several kilometers above the seismogenic zone) exhibits exponential scaling. We are capturing the behavior of the damage zone at large length scales and show that the exponential decay relationship extends to at least 10^3 m length scale from the central fault strand.

4.3. Damage zone width

The data indicate the half width of the Palos Verdes Fault is 2 km, or 4 km total width. The width determined is indicated by the clear break in slope shown in Fig. 5 defining a clear boundary between the fault and the relatively undisturbed basin to the east. As shown in Table 1 and Fig. 6, there is an apparent tradeoff between the decay of fault and fracture probability with distance and the fracturability of the background that result in a surprising stability of the damage zone width throughout different depths and lithologies. The intersection of the damage trend with the background occurs at ~2 km from the center of the fault for all layers that differ in composition, age, and depth (Fig. 6). This indicates that the overall along-strike average (17 km along strike) width is instead a function of an attribute intrinsic to the Palos Verdes Fault (e.g., length, fault maturity, or number of active strands). The damage zone width identified here is wider than may be inferred from studies of the damage zone width's dependence on displacement (Figure S8).

The width identified in this study is slightly wider than the 1-2 km widths inferred in some passive seismic tomographic studies (Thurber et al., 1997; Cochran et al., 2009; Yang et al., 2011). These studies approximate the damage zone as a zone with up to

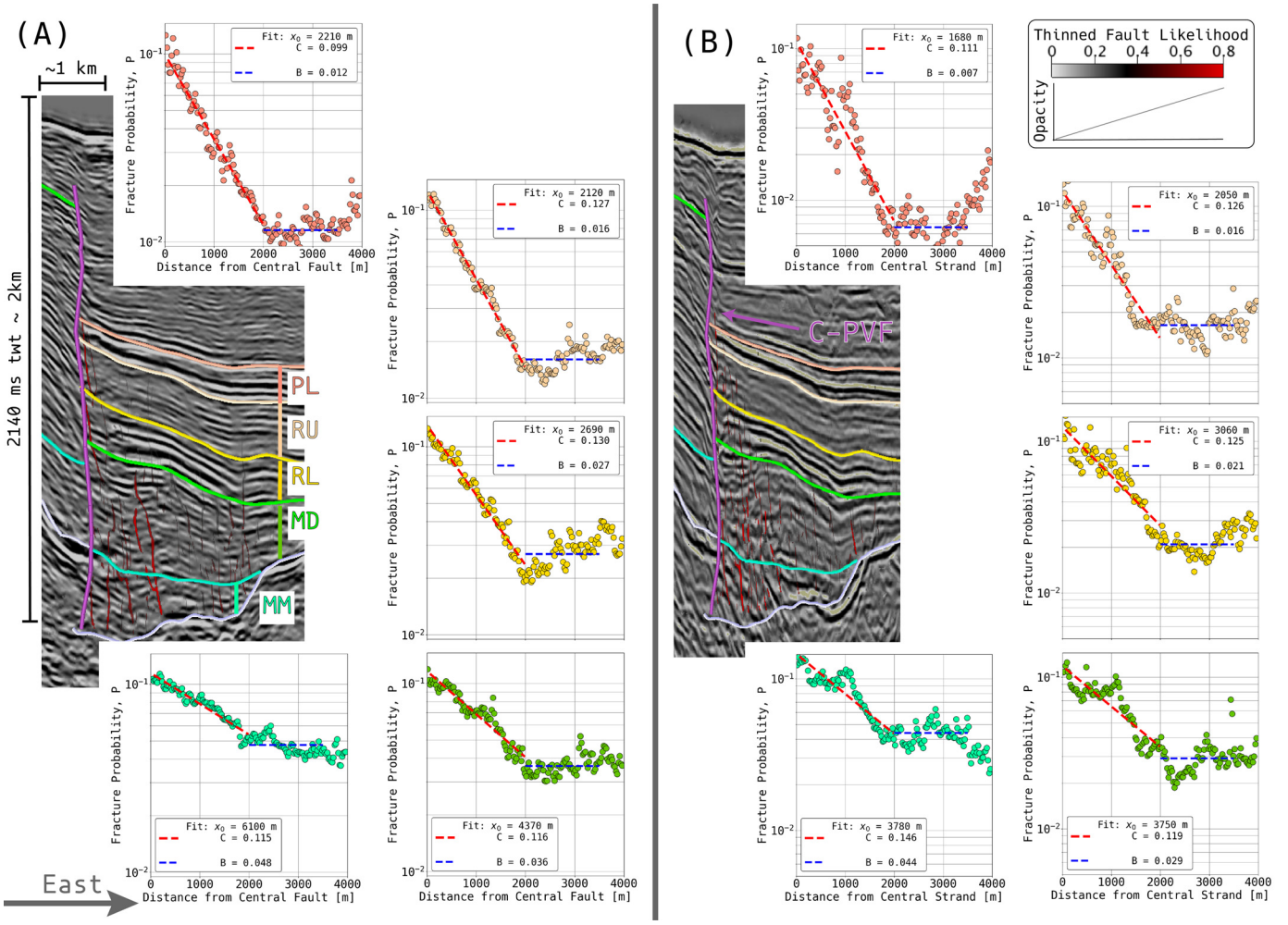

Fig. 6. The left side of each figure shows a representative example of dip-steered diffusion filtered seismic inline 1340 data in black and white color scale (line location shown in Fig. 1). The overlain vertical purple line represents the manually mapped central strand. The transparent to red is the thinned fault likelihood fault detections and transparency indicated. The multi-color horizontal lines are mapped three-dimensional (3D) horizon-surfaces and mark lithological contacts or unconformities that have been tied to well logs (PL - Pico lower, RU - Repetto upper, RL - Repetto lower, MD - Monterey Delmontian, MM - Monterey Mohnian). These horizons are used as upper and lower bounds to constrain the fracture probability as a function of distance away from the fault for each lithology in full 3D space, not just at the example inline. (A) are the Chevron volume results, which are shown in the semi-log plots on the right of the seismic line, colors match the lithology units indicated on the seismic line, and data are averaged over - 17 km along strike. (B) shows the results for the Shell volume and are averaged over 4.5 km. Note the different exponential fit slopes (red line) and background (blue line) for each geologic unit (horizontal portion).

50% reduction in P and S wave velocities, that extend to depths of at least 5 km. These studies also find an increase in Vp/Vs ratios within the seismically identified damage zone suggesting that the fractured damage zone is fluid filled. The similar width of these studies to our present study is reassuring given the differences in methods and resolution (tomographic grid sizes are typically $\sim 1 \times 1$ km compared to bin sizes of 50×25 m and 25×12.5 m in this study, see Supplement). The passive seismic studies hinge on seismic body wave ray paths to sample the fault zone and thus are limited in their resolution and spatial sampling. In contrast the present study has uniform sampling throughout, thus may be more resolving of the outer bounds of the damage zone. In addition, tomography studies use deviations in wave speed that may evolve with fault healing as a proxy for damage, whereas in our study we use high fold (high source/receiver sampling) direct reflection imaging to identify the damage zone. We are directly imaging the damage associated with the fault, through reflection discontinuities and abrupt changes in amplitude character, and propose that this method may be more sensitive to more subtle damage and thus delineates a wider damage zone.

Our measurements of fault zone width are also larger than those inferred from passive seismic studies that utilize fault-zone trapped head waves that are critically reflected at the boundary between damaged and undamaged rock (Li et al., 1997; Ben-Zion et al., 2003; Li et al., 2004; Yang et al., 2014; Li et al., 2016a,b). These studies find a narrower, several hundred-meter-wide damage zone, that extend to at least 5 km depth. One could speculate that the fault zone trapped wave is sampling the width of an inner fault damage zone rather than the outer edge of the fault damage zone. Lewis and Ben-Zion (2010) showed that fault trapped waves are not ubiquitous along strike in the mature (Parkfield) section of the San Andreas Fault. These studies rely on forward modeling of the waveform and travel times and may be non-unique in their parametrization (Ben-Zion, 1998). In addition, the inherently sparsity of passive seismic studies leads to spatial averaging of parameters.

The damage zone width in this study is about a factor of two wider than the 2-km compliant off fault damage zones inferred in other studies based on geodetic measurements (Fialko et al., 2002; Fialko, 2004). The geodetic studies used the response of terrestrial strike-slip faults to nearby earthquakes to infer reduced elastic moduli near the faults that were interpreted as indicative of damage zones. Like in this study, the geodetically inferred damage zones on the order of kilometers.

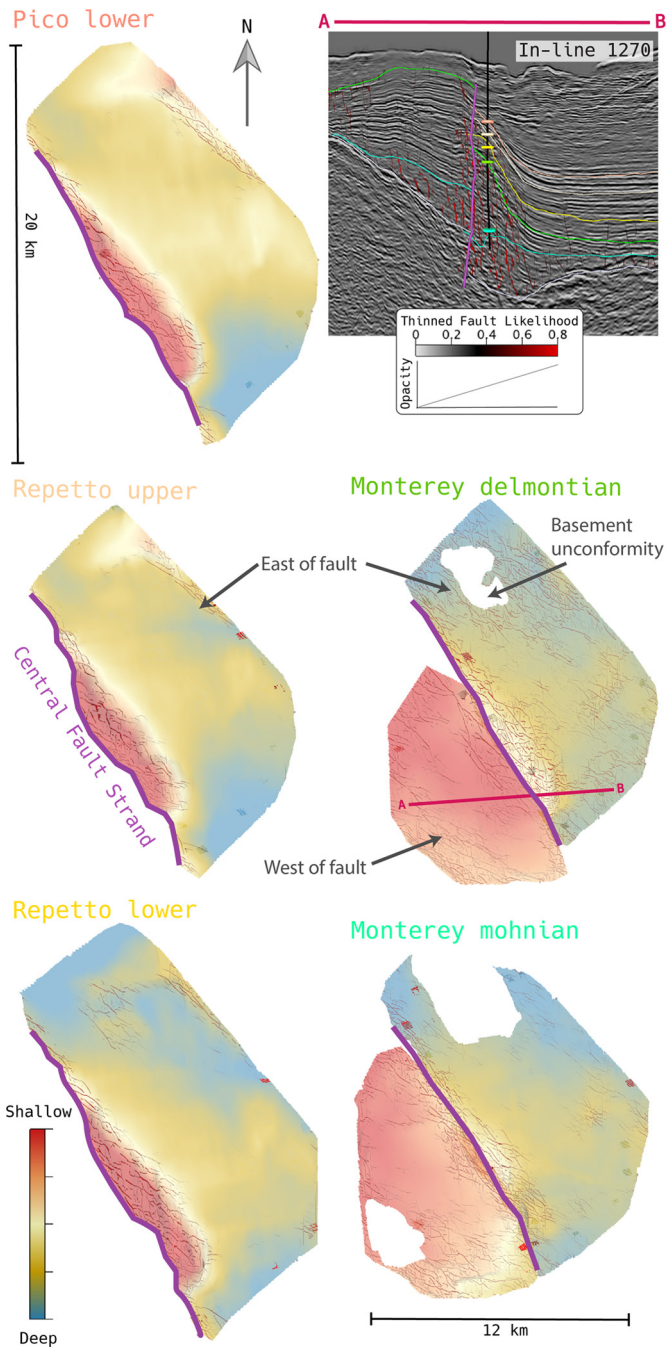

Fig. 7. Showing the results of thinned fault likelihood fault detection projected on mapped three-dimensional (3D) horizons, shown in map view. The thinned fault likelihood color map grades from transparent at 0 to red at 0.8 chosen to highlight the localization around the fault. The color map on the Chevron horizon surfaces ranges from red to blue, indicating shallow to deep in two-way travel time relative to each layer. The horizons have been cropped in-lines (500-1400) and crosslines (950-1900). The central fault strand is colored purple, the western fault strand in dark purple, and the eastern fault strand in navy blue. (Upper right) inset shows a Shell volume inline 1270 (location shown in Fig. 1) cross-section through the data where the gray scale seismics that have dip-steered diffusion filtering applied. The colored lines represent mapped horizons, and the colors correspond to the labels on the map view horizons.

Most geologic outcrop studies find a narrower fault damage zone width than the present study. Outcrop studies are a direct ground truth of the geology; however, exhumed surficial exposures are scarce, limited in scope, and transects are 1D in most cases. We speculate that many of these studies are missing the outer edge of many superposed damage zones, and in some cases may misinterpret a local minimum in damage as the background fracture density (outer limit of the damage zone). In many cases exposure and sampling prohibit observation of the true damage zone edge, which we find to be several kilometers from the fault core along the Palos Verdes Fault.

The damage zone width in this study is similar to the width identified in another active source attribute study of a strike slip damage zone (Liao et al., 2019). Liao et al. (2019) found a damage zone width of ~1600 m using structurally oriented seismic coherence (analogous to semblance) of the El Reno Fault in Oklahoma and fit an exponential to their data (Figure S9). The approach of the Liao et al. (2019) study maps coherence on 11 2D cross sections in an on-land 3D seismic volume of similar spatial resolution to this study (bin spacing 33.5 × 33.5 m) and show 2 distinct along strike trends that are fit with an exponentials that decay more steeply with distance from the fault than our analysis (Figure S9). The discrepancy in the width between these two studies may be due to the maturity of the faults. The El Reno Fault is 32 km in length and the Palos Verdes Fault is 100 km. Another similar study of 6 immature normal faults (<3 km in length and 100 s of meters of displacement) in the Bohai Bay Basin in China, which also used similarity-based attributes on 2D cross sections in 3D volumes, found damage zones in the range of 200–400 m (Liao et al., 2020). Their damage decay with distance was fit using a power law, and the comparatively narrower damage zone width is again potentially a function of fault maturity.

4.4. Sedimentary rock and damage

Lithology along the Palos Verdes Fault appears to play a role in the decay of fracture probability with distance from the fault and the level of background fracturing. The background fracture probability (stable region beyond 2 km) increases with increasing stratigraphic depth. Background fracture probability generally increases from shallow to deep. This result suggests that the first-order impact of damage in sedimentary rock in depths ranging from 400–2000 m is determined by depth, age, or fault growth. The systematic change in damage decay and background with increased depth and normal stress may support the prediction that damage is controlled by confining pressure from of overburden (Scholz, 2000).

The Monterey Formations (Delmontian and Mohnain) are the thickest and have the greatest integrated damage. One plausible explanation could be the effect of unit thickness on joint spacing correlation (Hobbs, 1967; Narr and Suppe, 1991). Large joint or fault spacing could be more detectable with seismic methods, however, the overlying lower Repetto Formation is one of the thinnest units and has high integrated damage. Alternatively, the documented enhanced brittleness intrinsic to the Monterey Formation (Eichhubl and Behl, 1998; Behl, 1999; Eichhubl and Boles, 2000) may allow it to accumulate more damage. Additionally, these formations have experienced more cumulative displacement, thus accumulating more damage.

The importance of geology on fault damage has been suggested (Caine et al., 1996; Shipton and Cowie, 2003; Kim et al., 2004; Berg and Skar, 2005). However, it is not clear how lithology impacts the damage trends in this study. Here the units are all siliciclastic sedimentary rock and maybe too similar to differentiate a lithologic dependence at the resolution in this study.

4.5. East versus West comparison

It has been argued that observations of a broad distributed damage zone are a result of the superposition of multiple subparallel fault strands with a cumulative effect resulting in a wider

Table 1
Providing values for parameters x0 and C fit by equation (1), background level B, and descriptions of applicable lithologies.

Data	x0 (m)	+/−	B	+/−	C	+/−	Description
Chevron volume	3540	64	0.027	0.0002	0.118	0.001	Complete volume from Pico to basement
- Pico – lower	2210	48	0.012	0.0002	0.1	0.003	Pliocene interbedded silt and sandstone
- Repetto upper	2120	27	0.016	0.0003	0.127	0.002	Pliocene sandstone and conglomerate
- Repetto lower	2690	72	0.027	0.0006	0.13	0.003	Pliocene medium to coarse sandstone and siltstone
- Monterey Delmontian	4370	172	0.033	0.0006	0.116	0.002	Miocene diatomaceous & high silica
- Monterey Mohnian	6100	251	0.047	0.0006	0.115	0.002	Miocene thinly bedded chert and shale
Shell volume	3200	115	0.033	0.0003	0.103	0.004	Compete volume from Pico to basement
- Pico – lower	1680	67	0.007	0.0002	0.111	0.008	Pliocene interbedded silt and sandstone
- Repetto upper	2050	70	0.016	0.0004	0.126	0.006	Pliocene sandstone and conglomerate
- Repetto lower	3060	195	0.021	0.0005	0.125	0.007	Pliocene medium to coarse sandstone and siltstone
- Monterey Delmontian	3750	206	0.029	0.0011	0.119	0.005	Miocene diatomaceous & high silica
- Monterey Mohnian	3700	176	0.044	0.0009	0.146	0.005	Miocene thinly bedded chert and shale

zone of damage (Mitchell and Faulkner, 2009; Savage and Brodsky, 2011). Our data may support this model because there are at least 3 continuously mappable fault strands and other subsidiary strands identified by the algorithm. We find a particularly smooth decay of damage with distance (Fig. 5 & 6) in the Chevron volume that is averaged over longer along strike distances (∼17 km) and more variability in the decay trends in the Shell volume that represents a shorter fault length (∼4.5 km). There is a distinct peak in fracture probability at 1 km distance from the central fault strand in the Shell volume (Fig. 5, 6 & 8) that corresponds to the eastern fault strand that has been previously documented (Walton et al., 2020). This additional fault strand is apparent in the portion on Chevron data that overlaps Shell volume (Figure S10). Resolving multiple fault strands suggests that the damage zone superposition model is likely accurate, and that the additive impact of multiple anastomosing secondary fault strands and associated damage zones creates a smooth decay.

The variability of the damage decay trend at shorter distances makes comparing east versus west a bit tenuous; however, it is clear that on both sides of the fault fracture probability decreases with distance from the central fault strand. The decay on both sides may be fit with an exponential, and for the 4.5 km fault length segment that displays a clear influence from the eastern fault (right side of Fig. 8), we can fit the western trend and the outside of the eastern fault strand with roughly the same parametrization. One could argue that the similarity in the decay trends tells us that both strands have a similar faulting history (displacement, number of slip events, etc.) or that these two strands have similar damage decays independent of their history, though this effect cannot be determined from the data. Finally, we find that the background fracture probability is higher on the west side of the fault. We think that this could be due to the increased deformation associated with the Palos Verdes anticline uplift that includes more time integrated tectonic damage.

4.6. Folding and damage

Like most faults, the Palo Verdes is accompanied by folding yet our discussion thus far has only focused on the faulting and its brittle damage. Visual inspection of the data (e.g., Fig. 3, 7 or 8) suggests that the edge of the fold abutting the fault corresponds to the edge of the damage at about 2.1 km from the central strand (Fig. 9). We can further refine this initial observation by measuring dip and comparing it to damage. Specifically, we calculate polar dip in full 3D space at each voxel using inline and crossline dips calculated in section 3.1 with dip steering (Tingdahl and De Rooij, 2005) and utilize the square root of the sum of the squared inline and crossline dips. This provides us with the magnitude of the apparent dip since the seismic volumes are in time, and dips are in units of [us/m]. This provides the magnitude of the dip, but no direction information; however, the morphology of the bedding contacts is simple and generally dips to the northeast with dip decreasing away from the fault (Fig. 7.) Fig. 9 reinforces the inference that the fold and damage are co-located.

Thus, some natural questions emerge about the relationship between the damage and folding. Is the damage only indirectly controlled by the fault and more directly created by the fault-generated fold? Alternatively, is the extent of the fold controlled by the extent of the weakened, damaged zone?

If the folding is the direct cause of the damage, we would expect the damage to be tensile and highest where the strain produced by folding is highest. The detected damage features are sub-vertical, thus a sub horizontal tensile strain would be required. Folding produces such strains that are proportional to curvature. The data do not support this possibility. Fig. 9 suggests that curvature is not well-correlated with damage in this particular 2D

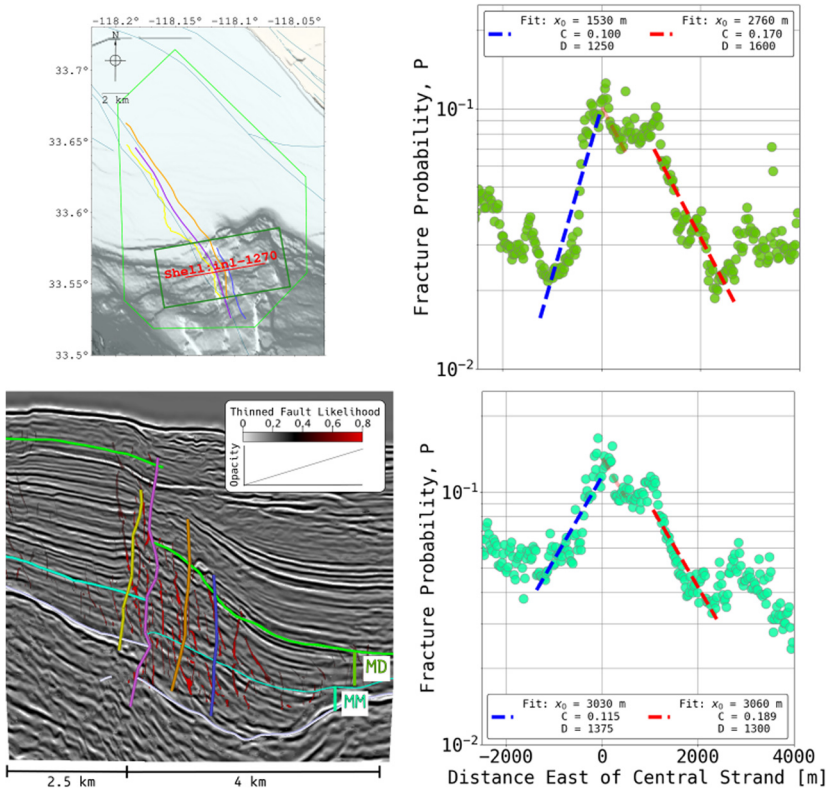

Fig. 8. Showing fracture probability as a function east of the central fault strand. The inset map in the upper left shows the bounds of the shell volume in dark green which the data are averaged over. The solid yellow, purple, orange, and blue lines on the map show the western, central, eastern, and eastern 2 fault traces respectively. The dark redline indicates the location of the example seismic line below (lower right). Where the mapped green (MD – Monterey Delmontian) and cyan (MM – Monterey Mohnian) sub horizontal lines indicate the unit boundaries or unconformities, mapped to the central fault strand shown as the sub vertical purple line. The top plots with green circles are the Monterey Delmontian Formation. The middle panels show example inlines for the volumes, indicated on the map. The bo–tom plots with teal circles show the fracture probability results for Monterey Mohnian Formation. See text for more details.

section. In fact, the edge of the fold is the locale of highest curvature, and it corresponds to reduction, rather than increase, of damage.

This preliminary interpretation is supported by a more thorough analysis considering the potential 3D aspect of the geometry (Fig. 9). The mean curvature (mean of the maximum and minimum curvatures) is an appropriate measure for this situation (Roberts, 2001). An alternative metric would be Gaussian curvature (Lisle, 1994), but Gaussian curvature is inappropriate for a cylindrical fold because it is very unstable when the minimum curvature measure is close to zero (Mynatt et al., 2007; Nabavi and Fossen, 2021). Here we calculate mean curvature in a spatial kernel of 10 inline and crossline bins assuming a constant velocity of 2,500 m/s. Other velocities and spatial kernels were tested and did not change the results. We compare the along strike averaged mean curvature to fracture probability from section 3.4 (Fig. 9). The results reinforce the preliminary interpretation. The curvature is not highest where the damage is highest. The bending strains are unlikely to be the primary cause of the damage.

Instead, we suggest that the width fold is likely limited by the damage. Damage weakens the rock and makes it more susceptible to ductile deformation.

5. Conclusions and implications

Using three-dimensional (3D) seismic attribute techniques, we find that the fault damage zone is observable and identifiable in seismic reflection datasets collected along the Palos Verdes Fault, offshore southern California. The seismic attribute computed from the data is representative of the damage zone and areas with elevated fault and fracture probability are consistent with areas of mapped faults both in this study and independent fault mapping efforts.

Due to the large acquisition footprints and large amount of data, we extend observations to greater distances and with more continuous sampling than is typically possible at the outcrop scale and with increased resolution over passive seismic methods. Additionally, the large datasets allow for a well-defined background and edge of the damage zone, which is ∼2 km away from the central fault strand.

The method allows us to distinguish fracturing trends as a function of distance from the fault, lithology, and depth. We find that the level of fracturing decreases systematically with lateral distance from the fault. This trend is best fit by an exponential with a decay distance of between ∼2000 and 4000 m, depending on lithology. We find that lithological variations and depth have the strongest control on damage decay and background fracturing.

The new window into damage as a function of lithology and depth provides a new insight into the trade-off between background damage and decay. Interestingly, these factors counterbalance each other resulting in a consistent damage width across the units. The data indicate that width can be a more stable feature of damage zones than might be anticipated from observed variations and trends in individual units. This new observation invites future modeling work exploring the role of rock strength in controlling damage zone width. Apparently, the relationship involves non-trivial feedback mechanisms that need to be fully explored.

CRediT authorship contribution statement

Travis Alongi: Conceptualization, Data curation, Formal analysis, Investigation, Methodology, Software, Visualization, Writing –

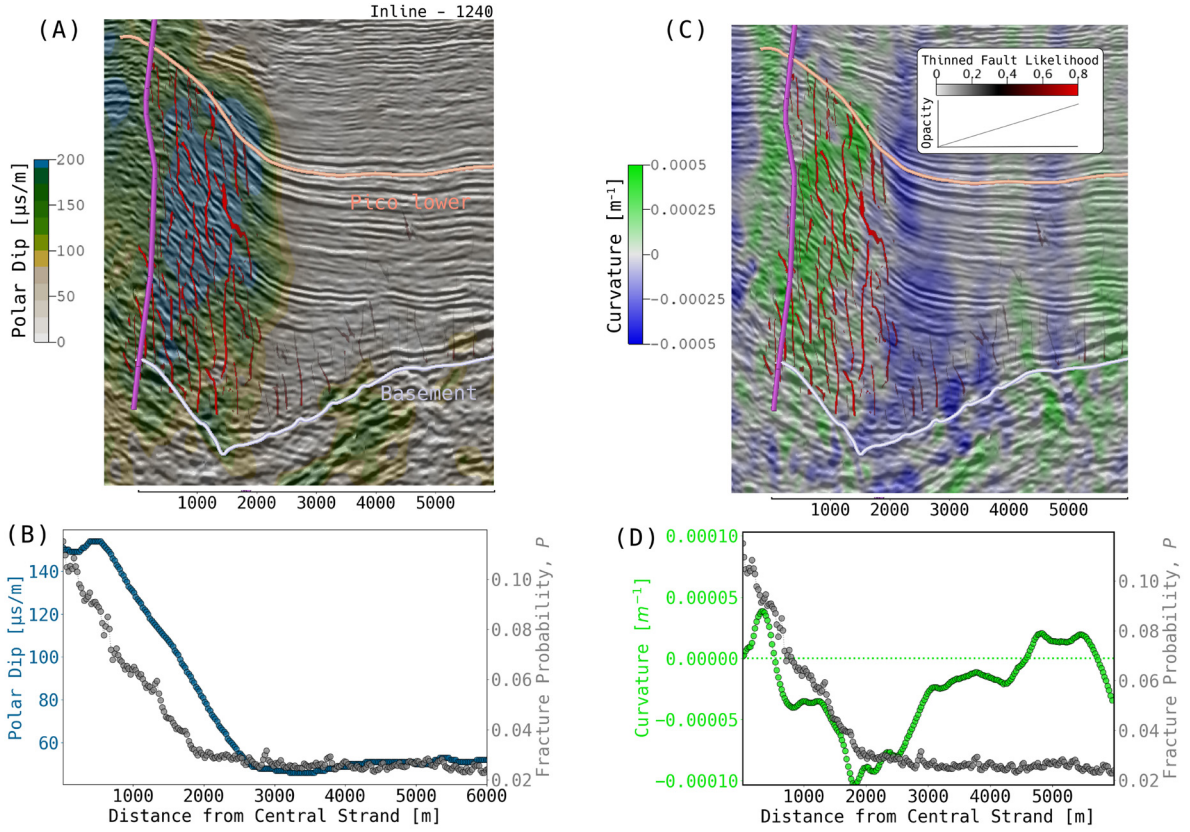

Fig. 9. Showing the correlation between the nearby fold and the damage zone. (A & C) shows a single two-dimensional ($2D$) example seismic inline with polar dip and curvature shown, respectively. Note, (B & D) are averaged over the volume. (A) depicts polar dip for the 2D example line where tan, green, blue color map transparency (50%) shows the calculated polar dip that decreases with distance from the fault into the sub-horizontal basin to the east. Overlain in transparent to red color are fault likelihood probabilities, displayed between the lower Pico horizon and the Basement that are shown in pink and light purple. The darker purple sub-vertical line is the central strand of the Palos Verdes Fault. (B) shows the binned along strike averaged values for polar dip in navy blue and fracture probabilities in gray. (C) same example seismic line as (A), where colormap (transparency 50%) green colors indicate negative curvature or concave down and blues indicate positive curvature or concave up. Overlain on the curvature colormap are the results for thinned fault likelihood. (D) is the along strike binned average mean curvature in green and fracture probabilities in gray. Note the most negative curvature makes the edge of the damage decay trend.

original draft. **Emily E. Brodsky:** Conceptualization, Funding acquisition, Project administration, Resources, Supervision, Writing – review & editing. **Jared Kluesner:** Data curation, Funding acquisition, Methodology, Project administration, Resources, Supervision, Visualization, Writing – review & editing. **Daniel Brothers:** Data curation, Funding acquisition, Resources, Supervision, Writing – review & editing.

Declaration of competing interest

The authors declare that they have no known competing financial interests or personal relationships that could have appeared to influence the work reported in this paper.

Data availability

Data used in study can be found at https://walrus.wr.usgs.gov/NAMSS/.

Acknowledgements

Seismic attribute analysis and interpretation were made possible with generous software donations from dGb (OpendTect) and Schlumberger (Petrel). We also thank Mark Leung and the Bureau of Ocean and Energy Management for project support. This work benefited from helpful discussion with members of the UC Santa Cruz seismology laboratory and the USGS Pacific Coast Marine Science Center geohazards team. Seismic data can be accessed at https://walrus.wr.usgs.gov/NAMSS/. The paper was improved due to comments from Nathan Miller, Patricia Persaud, and an anonymous reviewer. The project was partially funded by the Southern California Earthquake Center (Award # 21182). Any use of trade, product, or firm names is for descriptive purposes only and does not imply endorsement by the U.S. Government.

Appendix A. Supplementary material

Supplementary material related to this article can be found online at https://doi.org/10.1016/j.epsl.2022.117871.

References

Abercrombie, R.E., Rice, J.R., 2005. Can observations of earthquake scaling constrain slip weakening? Geophys. J. Int. 162, 406–424. https://doi.org/10.1111/j.1365-246X.2005.02579.x.

Alcalde, J., Bond, C.E., Johnson, G., Ellis, J.F., Butler, R.W.H., 2017. Impact of seismic image quality on fault interpretation uncertainty. GSAT. https://doi.org/10.1130/GSATG282A.1.

Atwater, T., 1970. Implications of plate tectonics for the Cenozoic tectonic evolution of Western North America. Geol. Soc. Am. Bull. 81, 3513. https://doi.org/10.1130/0016-7606(1970)81[3513:IOPTFT]2.0.CO;2.

Bahorich, M., Farmer, S., 1995. 3-D seismic discontinuity for faults and stratigraphic features: the coherence cube. Lead. Edge 14 (10), 1053–1058.

Behl, R.J., 1999. Since Bramlette (1946): The Miocene Monterey formation of California revisited. Classic Cordilleran concepts: a view from California. Spec. Pap., Geol. Soc. Am. 338, 301–313.

Ben-Zion, Y., 1998. Properties of seismic fault zone waves and their utility for imaging low-velocity structures. J. Geophys. Res. 103, 12567–12585. https://doi.org/10.1029/98JB00768.

Ben-Zion, Y., Peng, Z., Okaya, D., Seeber, L., Armbruster, J.G., Ozer, N., Michael, A.J., Baris, S., Aktar, M., 2003. A shallow fault-zone structure illuminated by trapped waves in the Karadere-Duzce branch of the North Anatolian Fault, western Turkey. Geophys. J. Int. 152, 699–717. https://doi.org/10.1046/j.1365-246X.2003.01870.x.

Berg, S.S., Skar, T., 2005. Controls on damage zone asymmetry of a normal fault zone: outcrop analyses of a segment of the Moab fault, SE Utah. J. Struct. Geol. 27, 1803–1822. https://doi.org/10.1016/j.jsg.2005.04.012.

Bohannon, R.G., Geist, E., 1998. Upper crustal structure and Neogene tectonic development of the California continental borderland. Geol. Soc. Am. Bull. 110, 779–800. https://doi.org/10.1130/0016-7606(1998)110<0779:UCSANT>2.3.CO;2.

Bonnet, E., Bour, O., Odling, N.E., Davy, P., Main, I., Cowie, P., Berkowitz, B., 2001. Scaling of fracture systems in geological media. Rev. Geophys. 39, 347–383. https://doi.org/10.1029/1999RG000074.

Botter, C., Cardozo, N., Hardy, S., Lecomte, I., Paton, G., Escalona, A., 2016. Seismicharacterizationn of fault damage in 3D using mechanical and seismic modelling. Mar. Pet. Geol. 77, 973–990.

Brankman, C.M., Shaw, J.H., 2009. Structural geometry and slip of the Palos Verdes Fault, Southern California: implications for earthquake hazards. Bull. Seismol. Soc. Am. 99, 1730–1745. https://doi.org/10.1785/0120080303.

Bramlette, M.N., 1946. The Monterey Formation of California and the Origin of Its Siliceous Rocks (vol. 212). US Government Printing Office.

Brothers, D.S., Conrad, J.E., Maier, K.L., Paull, C.K., McGann, M., Caress, D.W., 2015. The Palos Verdes Fault offshore Southern California: Late Pleistocene to present tectonic geomorphology, seascape evolution, and slip rate estimate based on AUV and ROV surveys. J. Geophys. Res., Solid Earth 120, 4734–4758. https://doi.org/10.1002/2015JB011938.

Brodsky, E.E., Mori, J.J., Anderson, L., Chester, F.M., Conin, M., Dunham, E.M., Yang, T., 2020. The state of stress on the fault before, during, and after a major earthquake. Annu. Rev. Earth Planet. Sci. 48 (1), 49–74.

Caine, J.S., Evans, J.P., Forster, C.B., 1996. Fault zone architecture and permeability structure. Geology 24, 1025. https://doi.org/10.1130/0091-7613(1996)024<1025:FZAAPS>2.3.CO;2.

Chester, F.M., Logan, J.M., 1986. Implications for mechanical properties of brittle faults from observations of the Punchbowl fault zone, California. Pure Appl. Geophys. PAGEOPH 124, 79–106. https://doi.org/10.1007/BF00875720.

Chester, J.S., Chester, F.M., Kronenberg, A.K., 2005. Fracture surface energy of the Punchbowl fault, San Andreas system. Nature 437, 133–136. https://doi.org/10.1038/nature03942.

Childs, C.J.J.P., Walsh, J.J., Watterson, J., 1997. Complexity in Fault Zone Structure and Implications for Fault Seal Prediction. Norwegian Petroleum Society Special Publications, vol. 7. Elsevier, pp. 61–72.

Choi, J.-H., Edwards, P., Ko, K., Kim, Y.-S., 2016. Definition and classification of fault damage zones: a review and a new methodological approach. Earth-Sci. Rev. 152, 70–87. https://doi.org/10.1016/j.earscirev.2015.11.006.

Chopra, S., Marfurt, K.J., 2005. Seismic attributes—a historical perspective. Geophysics 70 (5), 3SO–28SO.

Chopra, S., Marfurt, K., 2008. Gleaning Meaningful Information from Seismic Attributes, vol. 26, p. 11.

Cochran, E.S., Li, Y.-G., Shearer, P.M., Barbot, S., Fialko, Y., Vidale, J.E., 2009. Seismic and geodetic evidence for extensive, long-lived fault damage zones. Geology 37, 315–318. https://doi.org/10.1130/G25306A.1.

Cowie, P.A., Shipton, Z.K., 1998. Fault tip displacement gradients and process zone dimensions. J. Struct. Geol. 20, 983–997. https://doi.org/10.1016/S0191-8141(98)00029-7.

Crouch, J.K., Suppe, J., 1993. Late Cenozoic tectonic evolution of the Los Angeles basin and inner California borderland: a model for core complex-like crustal extension. Geol. Soc. Am. Bull. 105 (11), 1415–1434.

Dunham, E.M., Belanger, D., Cong, L., Kozdon, J.E., 2011. Earthquake ruptures with strongly rate-weakening friction and off-fault plasticity, Part 1: planar faults. Bull. Seismol. Soc. Am. 101 (5), 2296–2307.

Eichhubl, P., Behl, R.J., 1998. Diagenesis, Deformation and Fluid Flow in the Miocene Monterey Formation; Frontmatter and Roadlog.

Eichhubl, P., Boles, J.R., 2000. Focused fluid flow along faults in the Monterey Formation, coastal California. Geol. Soc. Am. Bull. 13.

Faulkner, D.R., Jackson, C.A.L., Lunn, R.J., Schlische, R.W., Shipton, Z.K., Wibberley, C.A.J., Withjack, M.O., 2010. A review of recent developments concerning the structure, mechanics and fluid flow properties of fault zones. J. Struct. Geol. 32, 1557–1575. https://doi.org/10.1016/j.jsg.2010.06.009.

Faulkner, D.R., Lewis, A.C., Rutter, E.H., 2003. On the internal structure and mechanics of large strike-slip fault zones: field observations of the Carboneras fault in southeastern Spain. Tectonophysics 367, 235–251. https://doi.org/10.1016/S0040-1951(03)00134-3.

Fialko, Y., Sandwell, D., Agnew, D., Simons, M., Shearer, P., Minster, B., 2002. Deformation on nearby faults induced by the 1999 Hector Mine earthquake. Science 297 (5588), 1858–1862.

Fialko, Y., 2004. Probing the mechanical properties of seismically active crust with space geodesy: study of the coseismic deformation due to the 1992 Mw7. 3 Landers (southern California) earthquake. J. Geophys. Res., Solid Earth 109 (B3).

Fisher, M.A., Normark, W.R., Langenheim, V.E., Calvert, A.J., Sliter, R., 2004. The offshore Palos Verdes fault zone near San Pedro, southern California. Bull. Seismol. Soc. Am. 94 (2), 506–530.

Hale, D., 2013. Methods to compute fault images, extract fault surfaces, and estimate fault throws from 3D seismic images. Geophysics 78, O33–O43. https://doi.org/10.1190/geo2012-0331.1.

Hauksson, E., Yang, W., Shearer, P.M., 2012. Waveform relocated earthquake catalog for Southern California (1981 to June 2011). Bull. Seismol. Soc. Am. 102, 2239–2244. https://doi.org/10.1785/0120120010.

Hobbs, D.W., 1967. The formation of tension joints in sedimentary rocks: an explanation. Geol. Mag. 104, 550–556. https://doi.org/10.1017/S0016756800050226.

Hubbard, J., Shaw, J.H., Dolan, J., Pratt, T.L., McAuliffe, L., Rockwell, T.K., 2014. Structure and seismic hazard of the Ventura avenue anticline and Ventura fault, California: prospect for large, multisegment ruptures in the western transverse ranges. Bull. Seismol. Soc. Am. 104, 1070–1087. https://doi.org/10.1785/0120130125.

Kim, Y.S., Peacock, D.C., Sanderson, D.J., 2004. Fault damage zones. J. Struct. Geol. 26 (3), 503–517.

King Hubbert, M., Rubey, W.W., 1959. Role of fluid pressure in mechanics of overthrust faulting: I. Mechanics of fluid-filled porous solids and its application to overthrust faulting. Geol. Soc. Am. Bull. 70 (2), 115–166.

Iacopini, D., Butler, R.W.H., Purves, S., McArdle, N., De Freslon, N., 2016. Exploring the seismic expression of fault zones in 3D seismic volumes. J. Struct. Geol. 89, 54–73. https://doi.org/10.1016/j.jsg.2016.05.005.

Keren, T.T., Kirkpatrick, J.D., 2016. The damage is done: low fault friction recorded in the damage zone of the shallow Japan Trench décollement. J. Geophys. Res., Solid Earth 121, 3804–3824. https://doi.org/10.1002/2015JB012311.

Kluesner, J.W., Brothers, D.S., 2016. Seismic attribute detection of faults and fluid pathways within an active strike-slip shear zone: new insights from high-resolution 3D P-Cable™ seismic data along the Hosgri Fault, offshore California. Interpretation 4 (1), SB131–SB148.

Lewis, M.A., Ben-Zion, Y., 2010. Diversity of fault zone damage and trapping structures in the Parkfield section of the San Andreas Fault from comprehensive analysis of near fault seismograms: diversity of fault zone damage at Parkfield. Geophys. J. Int. 183, 1579–1595. https://doi.org/10.1111/j.1365-246X.2010.04816.x.

Li, S., Freymueller, J., McCaffrey, R., 2016a. Slow slip events and time-dependent variations in locking beneath Lower Cook Inlet of the Alaska-Aleutian subduction zone. J. Geophys. Res., Solid Earth 121, 1060–1079. https://doi.org/10.1002/2015JB012491.

Li, Y., Catchings, R.D., Goldman, M.R., 2016b. Subsurface fault damage zone of the 2014 M w 6.0 South Napa, California, earthquake viewed from fault-zone trapped waves. Bull. Seismol. Soc. Am. 106, 2747–2763. https://doi.org/10.1785/0120160039.

Li, Y.G., Ellsworth, W.L., Thurber, C.H., Malin, P.E., Aki, K., 1997. Fault-zone guided waves from explosions in the San Andreas fault at Parkfield and Cienega Valley, California. Bull. Seismol. Soc. Am. 87 (1), 210–221.

Li, Y.-G., Vidale, J.E., Cochran, E.S., 2004. Low-velocity damaged structure of the San Andreas Fault at Parkfield from fault zone trapped waves: low-velocity damaged structure of the San Andreas Fault. Geophys. Res. Lett. 31. https://doi.org/10.1029/2003GL019044.

Liao, Z., Liu, H., Carpenter, B.M., Marfurt, K.J., Reches, Z.E., 2019. Analysis of fault damage zones using three-dimensional seismic coherence in the Anadarko Basin, Oklahoma. AAPG Bull. 103 (8), 1771–1785.

Liao, Z., Hu, L., Huang, X., Carpenter, B.M., Marfurt, K.J., Vasileva, S., Zhou, Y., 2020. Characterizing damage zones of normal faults using seismic variance in the Wangxuzhuang oilfield, China. Interpret. 8 (4), SP53–SP60.

Lisle, R.J., 1994. Detection of zones of abnormal strains in structures using Gaussian curvature analysis. AAPG Bull. 78, 1811–1819.

Ma, D.B., Wu, G.H., Scarselli, N., Luo, X.S., Han, J.F., Chen, Z.Y., 2019. Seismic damage zone and width–throw scaling along the strike-slip faults in the Ordovician carbonates in the Tarim Basin. Pet. Sci. 16 (4), 752–762.

Marfurt, K.J., Kirlin, R.L., Farmer, S.L., Bahorich, M.S., 1998. 3-D seismic attributes using a semblance-based coherency algorithm. Geophysics 63, 1150–1165. https://doi.org/10.1190/1.1444415.

Martel, S.J., Pollard, D.D., 1989. Mechanics of slip and fracture along small faults and simple strike-slip fault zones in granitic rock. J. Geophys. Res. 94, 9417. https://doi.org/10.1029/JB094iB07p09417.

McNeilan, T.W., Rockwell, T.K., Resnick, G.S., 1996. Style and rate of Holocene slip, Palos Verdes fault, southern California. J. Geophys. Res., Solid Earth 101, 8317–8334. https://doi.org/10.1029/95JB02251.

Mitchell, T.M., Faulkner, D.R., 2009. The nature and origin of off-fault damage surrounding strike-slip fault zones with a wide range of displacements: a field study from the Atacama fault system, northern Chile. J. Struct. Geol. 31, 802–816. https://doi.org/10.1016/j.jsg.2009.05.002.

Mynatt, I., Bergbauer, S., Pollard, D.D., 2007. Using differential geometry to describe 3-D folds. J. Struct. Geol. 29 (7), 1256–1266.

Nabavi, S.T., Fossen, H., 2021. Fold geometry and folding–a review. Earth-Sci. Rev. 222, 103812.

Narr, W., Suppe, J., 1991. Joint spacing in sedimentary rocks. J. Struct. Geol. 13, 1037–1048. https://doi.org/10.1016/0191-8141(91)90055-N.

Plesch, A., Shaw, J.H., Benson, C., Bryant, W.A., Carena, S., Cooke, M., Dolan, J., Fuis, G., Gath, E., Grant, L., Hauksson, E., Jordan, T., Kamerling, M., Legg, M., Lindvall, S., Magistrale, H., Nicholson, C., Niemi, N., Oskin, M., Perry, S., Planansky, G., Rockwell, T., Shearer, P., Sorlien, C., Suss, M.P., Suppe, J., Treiman, J., Yeats, R., 2007. Community Fault Model (CFM) for Southern California. Bull. Seismol. Soc. Am. 97, 1793–1802. https://doi.org/10.1785/0120050211.

Roberts, A., 2001. Curvature attributes and their application to 3 D interpreted horizons. First Break 19 (2), 85–100.

Rodriguez Padilla, A.M., Oskin, M.E., Milliner, C.W., Plesch, A., 2022. Accrual of widespread rock damage from the 2019 Ridgecrest earthquakes. Nat. Geosci. 15 (3), 222–226.

Sagy, A., Brodsky, E.E., 2009. Geometric and rheological asperities in an exposed fault zone. J. Geophys. Res. 114, B02301. https://doi.org/10.1029/2008JB005701.

Savage, H.M., Brodsky, E.E., 2011. Collateral damage: evolution with displacement of fracture distribution and secondary fault strands in fault damage zones. J. Geophys. Res. 116. https://doi.org/10.1029/2010JB007665.

Scholz, C.H., 2000. Evidence for a strong San Andreas fault. Geology 28, 163–166.

Scholz, C.H., Dawers, N.H., Yu, J.-Z., Anders, M.H., Cowie, P.A., 1993. Fault growth and fault scaling laws: preliminary results. J. Geophys. Res. 98, 21951–21961. https://doi.org/10.1029/93JB01008i.

Shaw, J.H., Suppe, J., 1996. Earthquake hazards of active blind-thrust faults under the central Los Angeles basin, California. J. Geophys. Res., Solid Earth 101, 8623–8642. https://doi.org/10.1029/95JB03453.

Shipton, Z.K., Cowie, P.A., 2003. A conceptual model for the origin of fault damage zone structures in high-porosity sandstone. J. Struct. Geol. 25, 333–344. https://doi.org/10.1016/S0191-8141(02)00037-8.

Shipton, Z.K., Soden, A.M., Kirkpatrick, J.D., Bright, A.M., Lunn, R.J., 2006. How Thick Is a Fault? Fault Displacement-Thickness Scaling.

Sorlien, C.C., Seeber, L., Broderick, K.G., Luyendyk, B.P., Fisher, M.A., Sliter, R.W., Normark, W.R., 2013. The Palos Verdes anticlinorium along the Los Angeles, California coast: implications for underlying thrust faulting: Palos Verdes Anticlinorium California. Geochem. Geophys. Geosyst. 14, 1866–1890. https://doi.org/10.1002/ggge.20112.

Tingdahl, K.M., De Rooij, M., 2005. Semi-automatic detection of faults in 3D seismic data. Geophys. Prospect. 53 (4), 533–542.

Thakur, P., Huang, Y., Kaneko, Y., 2020. Effects of low-velocity fault damage zones on long-term earthquake behaviors on mature strike-slip faults. J. Geophys. Res., Solid Earth 125 (8), e2020JB019587.

Thurber, C., Roecker, S., Ellsworth, W., Chen, Y., Lutter, W., Sessions, R., 1997. Two-dimensional seismic image of the San Andreas Fault in the Northern Gabilan Range, central California: evidence for fluids in the fault zone. Geophys. Res. Lett. 24, 1591–1594. https://doi.org/10.1029/97GL01435.

Torabi, A., Alaei, B., Kolyukhin, D., 2017. Analysis of fault scaling relations using fault seismic attributes: analysis of fault scaling relations. Geophys. Prospect. 65, 581–595. https://doi.org/10.1111/1365-2478.12440.

Torabi, A., Berg, S.S., 2011. Scaling of fault attributes: a review. Mar. Pet. Geol. 28, 1444–1460. https://doi.org/10.1016/j.marpetgeo.2011.04.003.

Triezenberg, P.J., Hart, P.E., Childs, J.R., 2016. National Archive of Marine Seismic Surveys (NAMSS)—A USGS Data Website of Marineseismic Reflection Data Within the U.S. Exclusive Economic Zone (EEZ). U.S. Geological Survey. https://walrus.wr.usgs.gov/NAMSS/.

Vidale, J.E., Li, Y.-G., 2003. Damage to the shallow Landers fault from the nearby Hector Mine earthquake. Nature 421, 524–526. https://doi.org/10.1038/nature01354.

Walton, M.A.L., Papesh, A.G., Johnson, S.Y., Conrad, J.E., Brothers, D.S., 2020. Quaternary faults offshore of California: U.S. Geological Survey data release. https://doi.org/10.5066/P91RYEZ4.

Ward, S.N., Valensise, G., 1994. The Palos Verdes terraces, California: Bathtub rings from a buried reverse fault. J. Geophys. Res. 99, 4485–4494. https://doi.org/10.1029/93JB03362.

Webb, T.H., Kanamori, H., 1985. Earthquake focal mechanisms in the eastern Transverse Ranges and San Emigdio Mountains, southern California and evidence for a regional decollement. Bull. Seismol. Soc. Am. 75 (3), 737–757.

Wilson, J.E., Chester, J.S., Chester, F.M., 2003. Microfracture analysis of fault growth and wear processes, Punchbowl Fault, San Andreas system, California. J. Struct. Geol. 25, 1855–1873. https://doi.org/10.1016/S0191-8141(03)00036-1.

Wong, T., 1982. Shear fracture energy of Westerly granite from post-failure behavior. J. Geophys. Res. 87, 990–1000. https://doi.org/10.1029/JB087iB02p00990.

Wright, T.L., 1991. Active margin basins. AAPG Mem. 52, 35–134.

Yang, H., Li, Z., Peng, Z., Ben-Zion, Y., Vernon, F., 2014. Low-velocity zones along the San Jacinto Fault, Southern California, from body waves recorded in dense linear arrays: damage zones of the San Jacinto Fault. J. Geophys. Res., Solid Earth 119, 8976–8990. https://doi.org/10.1002/2014JB011548.

Yang, H., Zhu, L., Cochran, E.S., 2011. Seismic structures of the Calico fault zone inferred from local earthquake travel time modelling: seismic structures of the Calico fault zone. Geophys. J. Int. 186, 760–770. https://doi.org/10.1111/j.1365-246X.2011.05055.x.

Yeats, R.S., Beall, J.M., 1991. Stratigraphic Controls of Oil Fields in the Los Angeles Basin. A Guide to Migration History. Chapter 7.